

# Unique Li Composite Anode with LiF on the Surface and Li-Sn Alloy Inside for Next Generation Li Metal Batteries

Zhifeng Xiao,<sup>[a]</sup> Jinbiao Chen,<sup>[a, b]</sup> Haitao Zhang,<sup>[a]</sup> Kaichen Yu,<sup>[a]</sup> Jie Li,<sup>\*[b]</sup> Xifang Li,<sup>[c]</sup> Abdullah N. Alodhayb,<sup>\*[d]</sup> and Zhicong Shi<sup>\*[a]</sup>

Lithium metal anode (LMA) is considered a promising anode with low electrochemical redox potential and ultrahigh theoretical specific capacity ( $3680 \text{ mAh g}^{-1}$ ) for next-generation high-energy batteries. However, the practical usage of LMA is still limited by the uncontrolled lithium dendrite growth, huge volume expansion, and low coulombic efficiency due to inhomogeneous lithium stripping/plating and side reactions with electrolytes. In this work, a unique Li composite anode (LiF-Li-Li<sub>22</sub>Sn<sub>5</sub>@Ni) is prepared for the first time via a facile one-step thermal fusion method. The LiF-Li-Li<sub>22</sub>Sn<sub>5</sub>@Ni anode consists of LiF on the surface, with Li-Sn alloy and Ni inside.

Among them, Sn serves as the lithiophilic site, which reduces the nucleation overpotential of lithium and inhibits the formation of dendrites. Ni, which is chemically inert to Li, can maintain the structural stability of the LiF-Li-Li<sub>22</sub>Sn<sub>5</sub>@Ni anode. Furthermore, the LiF on the surface can inhibit Li dendrite growth and induce uniform Li deposition. As a result, the performance of cell is remarkably improved, with more than 1500 hours of cycling in a symmetrical cell at  $1 \text{ mA cm}^{-2}$  for 1 hour, and a capacity retention of 88.4% after 800 cycles for the full cell assembled with LFP.

## Introduction

In the past decade, the rapid development of smart electronics, electric-powered vehicles, aviation, and renewable clean energy utilization, have significantly increased the demand for high-performance rechargeable batteries. In particular, the requirement for Li-ion batteries (LIBs) has increased, but the energy density of lithium-ion batteries in use today has been approaching the limit of its theoretical one,<sup>[1]</sup> so the lithium metal batteries (LMBs) using lithium metal as anode has begun to receive mass attention from scientists.<sup>[2,3]</sup>

Lithium metal anodes (LMA) possess a low electrode potential ( $-3.04 \text{ V}$  vs. the standard hydrogen electrode) and an exceptionally high theoretical specific capacity ( $3680 \text{ mAh g}^{-1}$ ),<sup>[4,5]</sup> which has been widely regarded as an ideal anode material for high-energy-density energy storage systems. However, the practical application of Li metal anodes still faces some problems. Li is a profoundly reactive metal, which leads to irreversible side reactions with electrolytes. The formation of

an uneven and uncontrolled solid electrolyte interface (SEI), results in continuous electrolyte consumption, leading to a decrease in coulombic efficiency (CE) and an increase in interfacial resistance.<sup>[6]</sup> Moreover, the "host less" deposition of  $\text{Li}^+$  will lead to serious dendrite growth and volume expansion during cycling, further exacerbating SEI rupture and recombination.<sup>[7]</sup> The uncontrolled dendrite growth will puncture the separator and cause an inner battery short circuit, which brings serious safety problems.<sup>[8]</sup>

Several strategies have been suggested to solve the severe issues of LMA, including electrolyte modification through the addition of appropriate additives to suppress dendrite growth,<sup>[9–12]</sup> the construction of an artificial SEI by *in-situ* or *ex-situ* methods to inhibit electrolyte decomposition, achieve perfect ionic conductivity, stabilize the SEI, and enhance ion and electron transport,<sup>[13–17]</sup> and the utilization of a three-dimensional current collector to alleviate volume expansion, because it can reduce local current density.<sup>[18–22]</sup>

All of the aforementioned techniques have demonstrated positive effects on dendrite inhibition and improvements in CE. Three-dimensional (3D) current collectors are able to successfully decrease local current density and limit the "infinite" volume expansion of lithium metal, stabilizing the Li stripping/plating process.<sup>[23–26]</sup> 3D current collectors typically use materials with good conductivity, such as Cu,<sup>[27]</sup> Ni,<sup>[28]</sup> or certain carbon material<sup>[29–31]</sup> which theoretically can facilitate uniform deposition of lithium metal. Nevertheless, their inherent characteristic, coupled with the significantly slower transfer rate of  $\text{Li}^+$  within the electrolyte compared to the rapid migration of electrons within the current collector, results in a preference for lithium ions to deposit preferentially on the collector's outer surface, rather than infiltrating deeper into the collector's structure.<sup>[32]</sup> Therefore, the most common way to improve the lithiophilic performance is to introduce lithiophilic sites on the collector

[a] Z. Xiao, J. Chen, H. Zhang, K. Yu, Z. Shi

*Institute of Batteries, School of Materials and Energy,  
Guangdong University of Technology, Guangzhou 510006, China*  
E-mail: zhicong@gdtu.edu.cn

[b] J. Chen, J. Li

*Department of Energy, Politecnico di Milano,  
Via Lambruschini, 4, Milan 20156, Italy*  
E-mail: jie1.li@polimi.it

[c] X. Li

*Beijing Dacheng School, Beijing 100141, China*

[d] A. N. Alodhayb

*Department of Physics and Astronomy, College of Science,  
King Saud University, Riyadh 11451, Saudi Arabia*  
E-mail: a.alodhayb@ksu.edu.sa

 Supporting information for this article is available on the WWW under  
<https://doi.org/10.1002/batt.202500031>

surface, such as Au,<sup>[33]</sup> Ag,<sup>[34]</sup> Sn,<sup>[35]</sup> Zn,<sup>[36]</sup> Co<sub>3</sub>O<sub>4</sub><sup>[37]</sup> and other lithophilic materials.<sup>[32,38,39]</sup> Lithophilic sites can appreciably improve the affinity of the current collector to Li metal, allowing Li to be evenly deposited in the current collector. LiF has high surface energy and a low energy barrier for Li<sup>+</sup> diffusion, it could be widely used to inhibit Li dendrite growth.<sup>[40–44]</sup> It has been reported that some metal fluorides, such as AlF<sub>3</sub><sup>[45]</sup> and ZnF<sub>2</sub>,<sup>[46]</sup> can react with lithium metal through high-temperature synthesis. This process results in a composite anode with a top layer composed of LiF and an interior made up of a lithium-friendly alloy 3D framework, which can efficiently improve the cycling performance of the lithium anode. Therefore, while improving the framework material, forming LiF as a protective coating on the surface of the LMA can adequately enhance the overall performance of the Li anode.

Herein, we designed a unique 3D Li metal composite anode named LiF-Li-Li<sub>22</sub>Sn<sub>5</sub>@Ni via a straightforward single-step thermal treatment process. Differing from prior research, LiF-Li-Li<sub>22</sub>Sn<sub>5</sub>@Ni has a spatial structure for outer LiF and inner continuous pore structure consisting of Li-Sn alloy and Ni (Li<sub>22</sub>Sn<sub>5</sub>@Ni). Sn is lithophilic, which allows it to form an alloy with lithium, and promote the Li uniform deposition by reducing the nucleation overpotential of Li<sup>+</sup>.<sup>[47]</sup> Ni is electrochemically inert to Li, allowing it to remain stable during the battery cycle.<sup>[48]</sup> The low Li-ion diffusion energy barrier and electronic insulating properties of LiF facilitate rapid Li<sup>+</sup> diffusion, promoting uniform Li<sup>+</sup> deposition.<sup>[49]</sup> The Li-Sn alloy generated by Sn and Li can reduce the nucleation overpotential of Li, diminish dendrite formation, and simultaneously form a framework with Ni to maintain the stability of the internal structure of the LiF-Li-Li<sub>22</sub>Sn<sub>5</sub>@Ni anodes. Consequently, the symmetric cells using the LiF-Li-Li<sub>22</sub>Sn<sub>5</sub>@Ni maintain the stability of the cycle for over 1500 h and demonstrate the outstanding performance of the full cells with LFP.

## Experimental

### Fabrication of LiF-Li-Li<sub>22</sub>Sn<sub>5</sub>@Ni

Nickel foam (NF) is alternately cleaned with DI water and alcohol three times and then dried for use. According to the mass ratio of Li: NF: SnF<sub>2</sub>=6: 3: 1, the appropriate amounts of Li, NF, and SnF<sub>2</sub> powders were taken in turn. The weighed Li was heated in a stainless-steel pan to 400 °C to melt completely, then the weighed NF and SnF<sub>2</sub> powders were added, and the mixture was mechanically stirred until the mixture was uniform in an argon (Ar)-filled glove box (H<sub>2</sub>O < 0.01 ppm, O<sub>2</sub> < 0.01 ppm). After cooling the mixture to environmental temperature, the resulting composite was rolled into 150-μm-thick foils, which were punched to be 10-mm-diameter disks and used as anodes in lithium metal batteries (LMBs), hereafter referred to as LiF-Li-Li<sub>22</sub>Sn<sub>5</sub>@Ni.

### Characterization

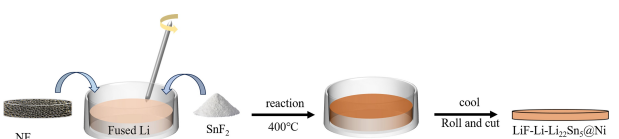
Scanning electron microscopy (SEM, Hitachi), operated at an accelerating voltage of 5–10 kV, was used to observe the morphology of pristine and cycled electrodes. Prior to the SEM test, the cycled electrodes were immersed in and rinsed with 1,3-Dioxolane (DOL) three times to remove surface residues. Elemental character-

istics is identified by energy-dispersive spectroscopy(EDS), and the EDS instrument is from Hitachi.X-ray diffraction (XRD, D8 ADVANCE) using a Cu K $\alpha$  radiation source at a wavelength of 0.1514 nm was used to characterize the structure of samples. All the specifically detected secondary ions were characterized by the time of flight secondary ion mass spectrometry (TOF-SIMSTESCAN GAIA3) with negative mode according to the relative sensitivity factors (RSF) value.

## Results and Discussion

The LiF-Li-Li<sub>22</sub>Sn<sub>5</sub>@Ni was obtained through a facile one-step thermal fusion method using lithium, SnF<sub>2</sub>, and NF (Scheme 1). The phase is consisting of the LiF-Li-Li<sub>22</sub>Sn<sub>5</sub>@Ni anode (Figure 1a, b, c). The XRD profile displays that the LiF-Li-Li<sub>22</sub>Sn<sub>5</sub>@Ni anode is composed of Li, Ni, LiF, and Li<sub>22</sub>Sn<sub>5</sub>. The diffraction peaks at 36.3°, 52.2°, and 64.9° correspond to the (110), (200), and (211) planes of Li (PDF#15-0401). Peaks observed at 44.5°, 51.8°, and 76.3° are attributed to the (111), (200), and (220) planes of Ni (PDF#04-0850). The peaks at 38.4°, 44.7°, and 65° correspond to the (111), (200), and (220) planes of LiF (PDF#71-4663), while the peaks at 22.1°, 23.6°, and 38.7° are assigned to the (422), (511), and (822) planes of Li<sub>22</sub>Sn<sub>5</sub> (PDF#18-0753).

The morphology and elemental characteristics of LiF-Li-Li<sub>22</sub>Sn<sub>5</sub>@Ni were identified using SEM and energy-dispersive spectroscopy (EDS). It can be discerned that the surface of the LiF-Li-Li<sub>22</sub>Sn<sub>5</sub>@Ni anode exhibits a dense granular structure (Figure 1d). Combined with EDS analysis, the results show an abundance of F uniformly distributed on the surface (Figure 1e), while Ni and Sn are found throughout the material (Figure 1f and g). The time-of-flight secondary ion mass spectrometry (TOF-SIMS) test was conducted to further investigate the spatial distribution of each component in the composite material. The



Scheme 1. Fabrication process of LiF-Li-Li<sub>22</sub>Sn<sub>5</sub>@Ni anode.

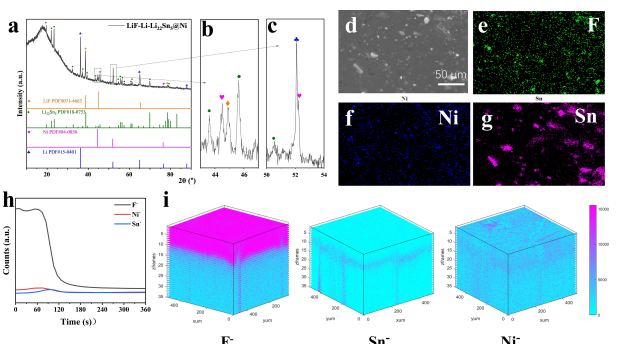


Figure 1. (a, b, c) XRD pattern of the LiF-Li-Li<sub>22</sub>Sn<sub>5</sub>@Ni anode before cycling. (d) Top-view SEM images and (e, f, g) the corresponding EDX elemental mapping image of the LiF-Li-Li<sub>22</sub>Sn<sub>5</sub>@Ni anode before cycling. (h) Depth profiling by sputtering time via TOF-SIMS. (i) The corresponding 3D reconstruction images of the TOF-SIMS signal detected for F-, Sn-, Ni-.

F elements are mainly concentrated on the surface of the LiF-Li<sub>22</sub>Sn<sub>5</sub>@Ni electrode,<sup>[50]</sup> and Sn and Ni elements are dispersed throughout the material (Figure 1h). In conjunction with the XRD test results, it is confirmed that the LiF is on the surface and Li<sub>22</sub>Sn<sub>5</sub> and Ni are in the inner of the composite anode, named as LiF-Li-Li<sub>22</sub>Sn<sub>5</sub>@Ni.

Galvanostatic measurements of symmetrical cells were used to estimate the performance of the LiF-Li-Li<sub>22</sub>Sn<sub>5</sub>@Ni. The long-term cycling performance of the bare Li and LiF-Li-Li<sub>22</sub>Sn<sub>5</sub> anodes in Li|Li symmetric cells was evaluated (Figure 2a). The symmetric cell with LiF-Li-Li<sub>22</sub>Sn<sub>5</sub>@Ni exhibits exceptional cycling stability at 1 mA cm<sup>-2</sup> and 1 mAh cm<sup>-2</sup> for over 1500 hours, maintaining a low polarization voltage of less than 30 mV. In contrast, the bare Li anode remained stable for less than 300 hours, exhibiting a significantly higher overpotential of 70 mV. The cycling lifetimes for the symmetric cells with LiF-Li-Li<sub>22</sub>Sn<sub>5</sub>@Ni were close to 340 h at a high current density of 3 mA cm<sup>-2</sup> and 1 mAh cm<sup>-2</sup> (Figure 2b). In comparison, the symmetric cells with bare Li demonstrate higher average potential hysteresis of about 100 mV and fail after 200 h.

EIS was performed to examine the interface characteristics of the bare Li and LiF-Li-Li<sub>22</sub>Sn<sub>5</sub>@Ni. This technique evaluates key parameters such as charge transfer resistance and ion conductivity at the electrode-electrolyte interface. The equivalent circuit model employed to fit the data is illustrated in Figure S1, the resistance of symmetric cells of bare Li (Table S1) and LiF-Li-Li<sub>22</sub>Sn<sub>5</sub>@Ni (Table S2) is reported at different cycles after fitness. The interfacial impedance ( $R_{SEI}$ ) of symmetric cells for Bare Li decreases from 171.90 Ω in the before cycle to 32.88 Ω after 50 cycles (Figure S2) and subsequently rises from 23.73 Ω in the 100th cycle to 50.08 Ω after 150 cycles (Figure 2c). This behavior may be attributed to the degradation and

subsequent reformation of the solid-electrolyte interphase (SEI) layer, coupled with the accumulation of "dead Li".<sup>[51,52]</sup> In contrast, the  $R_{SEI}$  of LiF-Li-Li<sub>22</sub>Sn<sub>5</sub>@Ni continuously decreases from 261.20 Ω in the before cycle to 1.71 Ω after the 150th cycle (Figure 2d, S2). Symmetric cells with LiF-Li-Li<sub>22</sub>Sn<sub>5</sub>@Ni exhibit stable interface impedance over multiple cycles, suggesting that the LiF-Li-Li<sub>22</sub>Sn<sub>5</sub>@Ni anode preserves a stable electrochemical interface and maintains its structural integrity. The LiF layer can enhance the stability of the electrode-electrolyte interface, because it can help to homogenize the Li-ion flux, the LiF-Li-Li<sub>22</sub>Sn<sub>5</sub>@Ni anode, compared to bare Li, demonstrates superior performance in maintaining interfacial stability and inhibiting dendrite growth during the deposition/stripping cycles.<sup>[44]</sup>

The cross-section of deposition of the LiF-Li-Li<sub>22</sub>Sn<sub>5</sub>@Ni and bare Li after 50 cycles were characterized to analyze the volume change by SEM. As shown in Figure 3, it is found that the deposited layer of bare Li (38.44 μm) is loose, porous, and fragmented. The deposited layer of the LiF-Li-Li<sub>22</sub>Sn<sub>5</sub>@Ni (33.80 μm) is significantly denser and smoother than that of the bare Li after 50 cycles, indicating that the LiF-Li-Li<sub>22</sub>Sn<sub>5</sub>@Ni can effectively improve behavior of Li depositing and decrease the volume expansion of the lithium metal anode during depositing.

To evaluate the effects of different anodes on lithium depositing, the surfaces of bare Li and LiF-Li-Li<sub>22</sub>Sn<sub>5</sub>@Ni disassembled from symmetric cells after 25 cycles were characterized using SEM. The surfaces of bare Li exhibit significant dendritic growth on both sides of Li depositing and stripping (Figure 4a and b). In contrast, no noticeable dendrites are growing on the surface of the depositing side of the LiF-Li-Li<sub>22</sub>Sn<sub>5</sub>@Ni (Figure 4c), and no residual dead lithium on the stripping side (Figure 4d).

After stripping to 2 mAh cm<sup>-2</sup> (Figure 4f) and 4 mAh cm<sup>-2</sup> (Figure 4g), the surface of LiF-Li-Li<sub>22</sub>Sn<sub>5</sub>@Ni anode reveals the continuous pore structure and when stripping to 6 mAh cm<sup>-2</sup>, SEM and the matching EDS profile clearly show the distribution of F, Sn, and Ni. Sn and Ni are mixed in the same area, while F is distributed throughout the image (Figure S3). This indicates that LiF can still maintain a stable composition on the negative electrode surface after separation, and the Li-Sn alloy and Ni are evenly distributed, forming the internal porous structure. Based on the above characterization, using lithium, SnF<sub>2</sub>, and Ni foam via a facile one-step thermal fusion method, we can obtain the LiF-Li-Li<sub>22</sub>Sn<sub>5</sub>@Ni anode, which exhibits a LiF surface and a pore structure, affording outstanding cycling performance.

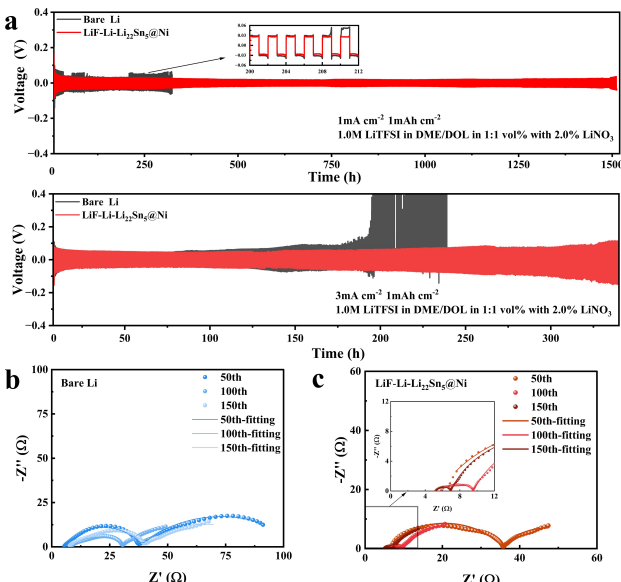


**Figure 2.** (a) Voltage-time profiles of symmetric cell with bare Li and LiF-Li-Li<sub>22</sub>Sn<sub>5</sub>@Ni using 1 M LiTFSI in DOL: DME = 1:1 vol% with 2% LiNO<sub>3</sub> at current densities of (a) 1 mA cm<sup>-2</sup> for 1 h, and (b) 3 mA cm<sup>-2</sup> for 20 min. Nyquist plots of symmetric cells with (c) bare Li and (d) LiF-Li-Li<sub>22</sub>Sn<sub>5</sub>@Ni electrodes during repeated cycles.

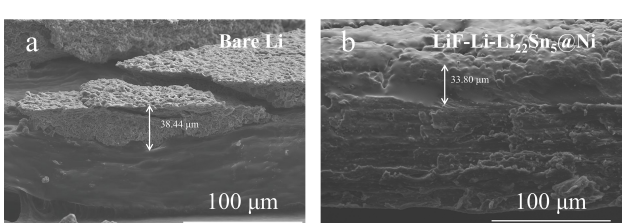


**Figure 3.** The cross-section of deposition of (a) LiF-Li-Li<sub>22</sub>Sn<sub>5</sub>@Ni and (b) bare Li after 50 cycles.

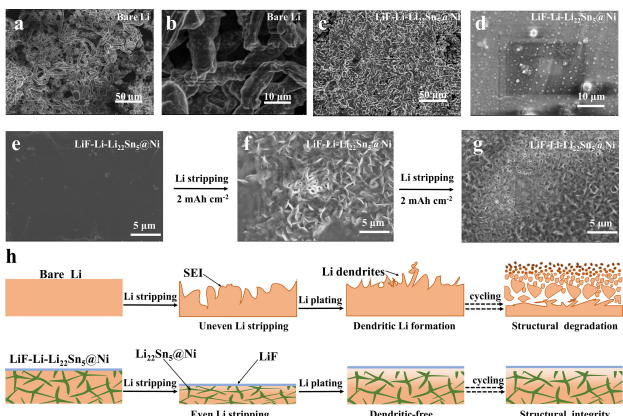


**Figure 4.** The top-view SEM images of the LiF-Li-Li<sub>22</sub>Sn<sub>5</sub>@Ni electrodes and bare Li electrodes at 25th cycle after Li deposition and Li stripping in condition of 1 mA cm<sup>-2</sup> and 1 mAh cm<sup>-2</sup> cycling, the plating side of (a) bare Li and (c) LiF-Li-Li<sub>22</sub>Sn<sub>5</sub>@Ni, the stripping side of (b) bare Li and (d) LiF-Li-Li<sub>22</sub>Sn<sub>5</sub>@Ni. Top-view SEM image of LiF-Li-Li<sub>22</sub>Sn<sub>5</sub>@Ni electrode after stripping (e) 0 mAh cm<sup>-2</sup> Li, (f) 2 mAh cm<sup>-2</sup> Li and (h) 4 mAh cm<sup>-2</sup> Li. (h) Schematic illustration of Li plating and stripping behaviors on bare Li anodes and the LiF-Li-Li<sub>22</sub>Sn<sub>5</sub>@Ni anodes.

ance in symmetric and full cells. First, the continuous porosity of Li<sub>22</sub>Sn<sub>5</sub>@Ni promotes electron/ion transport. Furthermore, it effectively optimizes the electric field distribution and reduces local current density for regular Li deposition, because the high specific surface area offers abundant nucleation sites. Additionally, the lithophilic Li–Sn alloy promotes the redeposition of free Li ions into nanopores. Third, the LiF surface homogenizes Li<sup>+</sup> deposition and improves the reliability of the interface for uniform Li deposition (Figure 4h).

To evaluate the practical potential of the LiF-Li-Li<sub>22</sub>Sn<sub>5</sub>@Ni anode, LFP was used as the cathode to assemble full cells, with the electrolyte consisting of 1 M LiPF<sub>6</sub> in DEC: EC = 1:1 Vol%. Before cycling at 4 C, all cells were activated with two initial cycles at 0.1 C. LFP || LiF-Li-Li<sub>22</sub>Sn<sub>5</sub>@Ni cell shows a discharge capacity of 90 mAh g<sup>-1</sup> and the capacity preservation rate of 88.4% after 800 cycles. While for LFP || bare Li, it experiences capacity decline starting from the 150th cycle and fails after 200 cycles (Figure 5a). At 2 C, after 300 cycles, the NCM811 || LiF-Li-Li<sub>22</sub>Sn<sub>5</sub>@Ni retains 85.2% of its capacity, whereas NCM811 || bare Li exhibits a capacity attenuation of 48.4% after 300 cycles, and its discharge capacity is also significantly lower than that of the battery using the LiF-Li-Li<sub>22</sub>Sn<sub>5</sub>@Ni anode (Figure 5b). The overpotential of the LFP || bare Li cells is significantly higher than that of the LFP || LiF-Li-Li<sub>22</sub>Sn<sub>5</sub>@Ni cells, as shown in the capacity-voltage curves (Figure 5c and d).

The rate performance of the full cells was assessed across a range of current rates, from 0.1 C to 10 C (Figure 6a). Under the low current rate of 0.1 C, the LFP || LiF-Li-Li<sub>22</sub>Sn<sub>5</sub>@Ni cell offers an initial discharge capacity of 160.9 mAh g<sup>-1</sup>. The capacity–voltage curves indicate that the overpotential of LFP || LiF-Li-Li<sub>22</sub>Sn<sub>5</sub>@Ni is lower than that of the LFP || bare Li cell (Figure 6b). The cell maintained stable discharge capacities of 148, 134, 118, 106, 96, 88, and 59 mAh g<sup>-1</sup>, as the current rate increased to 0.5 C, 1 C, 2 C, 3 C, 4 C, 5 C, and 10 C, respectively. These discharge capacities are consistently higher than those of the

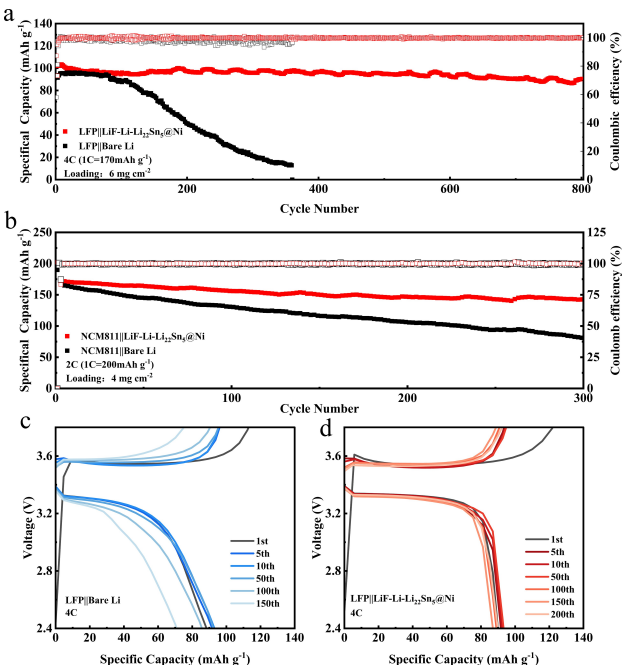


**Figure 5.** Cycling performance of LiF-Li-Li<sub>22</sub>Sn<sub>5</sub>@Ni -based full cells with (a) LFP at 4 C and (b) NCM811 at 2 C. Discharge–charge profiles with (c) LFP || bare Li and (d) LFP || LiF-Li-Li<sub>22</sub>Sn<sub>5</sub>@Ni at 4 C.

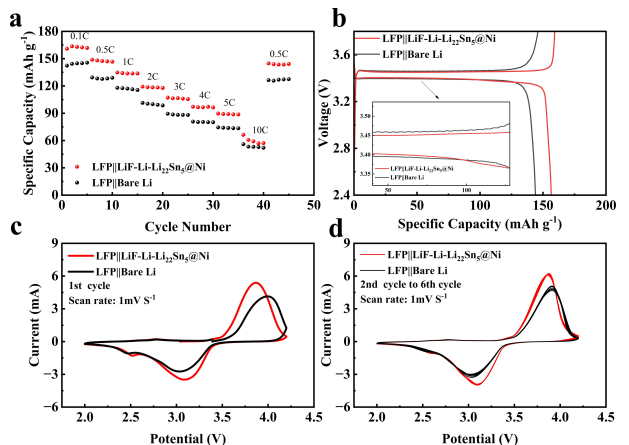


**Figure 6.** (a) Rate capability of the LFP || LiF-Li-Li<sub>22</sub>Sn<sub>5</sub>@Ni and LFP || bare Li full cells and (b) the corresponding voltage versus specific capacity profiles at 0.1 C. CV profiles of the LFP || bare Li and LFP || LiF-Li-Li<sub>22</sub>Sn<sub>5</sub>@Ni full cell: (c) the first cycle, (d) the 2nd cycle to the 6th cycle.

LFP || bare Li cell. Upon returning the current rate to the initial 0.5 C, the LFP || LiF-Li-Li<sub>22</sub>Sn<sub>5</sub>@Ni cell showed the retention of capacity is 98.7%, compared to the LFP || bare Li cell is 97.5%. These results suggest that the LFP || LiF-Li-Li<sub>22</sub>Sn<sub>5</sub>@Ni offers faster kinetics and better cyclic stability even under higher currents. The CV curves of LFP || LiF-Li-Li<sub>22</sub>Sn<sub>5</sub>@Ni cell maintained the same shape as LFP || bare Li from the first cycle to the sixth cycle, proving that there are no side reactions during the cycling process of the LiF-Li-Li<sub>22</sub>Sn<sub>5</sub>@Ni anode (Figure 6c, d). The higher current density and the reduced separation between oxidation and reduction peaks further confirm the enhanced

reversibility and superior Li-ion diffusion of LiF-Li-Li<sub>22</sub>Sn<sub>5</sub>@Ni as an LMA.

## Conclusions

In conclusion, in this work, we have successfully manufactured a unique LiF-Li-Li<sub>22</sub>Sn<sub>5</sub>@Ni anode with Li-Sn alloy inside and LiF on the surface through a straightforward one-step thermal treatment process. LiF are regularly dispersed on the LiF-Li-Li<sub>22</sub>Sn<sub>5</sub>@Ni anode surface, providing fast Li<sup>+</sup> diffusion paths, homogenizing Li<sup>+</sup> flux, and guiding regular Li<sup>+</sup> stripping/plating. The Li-Sn alloy can reduce the nucleation overpotential, and diminish dendrite formation. The continuous pore structure of Li<sub>22</sub>Sn<sub>5</sub>@Ni provides a large number of nucleation sites and reduces local current density during cycling. For this reason, the Li tends to deposit uniformly on the LiF-Li-Li<sub>22</sub>Sn<sub>5</sub>@Ni anode, resulting in a stable and smooth surface. The cycle life of the symmetric cells exceeds 340 h at 3 mA cm<sup>-2</sup> and 1 mAh cm<sup>-2</sup>, or 1500 h at 1 mA cm<sup>-2</sup> and 1 mAh cm<sup>-2</sup>. The full cells assembled with LiF-Li-Li<sub>22</sub>Sn<sub>5</sub>@Ni and LFP cathode provide a capacity retention of 88.4% after 800 cycles, and the capacity retention of NCM811||LiF-Li-Li<sub>22</sub>Sn<sub>5</sub>@Ni cells can maintain 85.2% after 300 cycles. This simple one-step thermal treatment method is easy and simple to operate, which is also suitable for other alkaline metal anodes.

## Acknowledgements

We gratefully acknowledge the financial support from the Ministry of Science and Technology of People's Republic of China (502220178), and the Researchers Supporting Project Number (RSP2025R304), King Saud University, Riyadh, Saudi Arabia. We wish to thank the Analysis and Test Center, Guangdong University of Technology for the microscopy and microanalysis.

## Conflict of Interests

The authors declare no conflict of interest.

## Data Availability Statement

The data that support the findings of this study are available from the corresponding author upon reasonable request.

**Keywords:** Lithium metal anode • Li composite anode • LiF • Li-Sn alloy

- [1] J. B. Goodenough, Y. Kim, *Chem. Mater.* **2010**, *22*(3), 587–603. <https://doi.org/10.1021/cm901452z>.
- [2] Z. Shen, J. Zhong, J. Chen, W. Xie, K. Yang, Y. Lin, J. Chen, Z. Shi, *Chin. Chem. Lett.* **2023**, *34*(3), 107370. <https://doi.org/https://doi.org/10.1016/j.ccl.2022.03.093>.

- [3] J. Liu, Z. Bao, Y. Cui, E. J. Dufek, J. B. Goodenough, P. Khalifah, Q. Li, B. Y. Liaw, P. Liu, A. Manthiram, Y. S. Meng, V. R. Subramanian, M. F. Toney, V. V. Viswanathan, M. S. Whittingham, J. Xiao, W. Xu, J. Yang, X. Q. Yang, J. G. Zhang, *Nat. Energy* **2019**, *4*(3), 180–186. <https://doi.org/10.1038/s41560-019-0338-x>.
- [4] W. Guo, S. Liu, X. Guan, X. Zhang, X. Liu, J. Luo, *Adv. Energy Mater.* **2019**, *9*(20), 1900193. <https://doi.org/https://doi.org/10.1002/aenm.201900193>.
- [5] Y. Fan, X. Chen, D. Legut, Q. Zhang, *Energy Storage Mater.* **2019**, *16*, 169–193. <https://doi.org/https://doi.org/10.1016/j.ensm.2018.05.007>.
- [6] X. Xie, L. Wei, J. Lu, A. Xu, B. Wang, X. Xiao, A. Wang, Z. Jin, Z. Shi, W. Wang, *Energy Storage Mater.* **2024**, *67*, 103323. <https://doi.org/https://doi.org/10.1016/j.ensm.2024.103323>.
- [7] Z. Shen, J. Huang, Y. Xie, D. Wei, J. Chen, Z. Shi, *ChemSusChem* **2024**, *17*(11), e202301777. <https://doi.org/https://doi.org/10.1002/cssc.202301777>.
- [8] Y. Cheng, J. Chen, Y. Chen, X. Ke, J. Li, Y. Yang, Z. Shi, *Energy Storage Mater.* **2021**, *38*, 276–298. <https://doi.org/https://doi.org/10.1016/j.ensm.2021.03.008>.
- [9] G. Zhang, X. Deng, J. Li, J. Wang, G. Shi, Y. Yang, J. Chang, K. Yu, S.-S. Chi, H. Wang, P. Wang, Z. Liu, Y. Gao, Z. Zheng, Y. Deng, C. Wang, *Nano Energy* **2022**, *95*, 107014. <https://doi.org/https://doi.org/10.1016/j.nanoen.2022.107014>.
- [10] C.-C. Su, J. Shi, R. Amine, M. He, S.-B. Son, J. Guo, M. Jiang, K. Amine, *Nano Energy* **2023**, *110*, 108335. <https://doi.org/https://doi.org/10.1016/j.nanoen.2023.108335>.
- [11] X. Zhang, Q. Wu, X. Guan, F. Cao, J. Xu, *J. Power Sources* **2020**, *452*, 227833, <https://doi.org/https://doi.org/10.1016/j.jpowsour.2020.227833>.
- [12] L. Zhai, W. Zhang, H. Gong, Y. Li, M. Gao, X. Zhang, D. Li, Y. Zhou, C. Dong, W. Liu, F. Jiang, J. Sun, *Surfaces and Interfaces* **2022**, *34*, 102299. <https://doi.org/https://doi.org/10.1016/j.surfin.2022.102299>.
- [13] J. Chen, D. Li, K. Lin, X. Ke, Y. Cheng, Z. Shi, *J. Power Sources* **2022**, *540*, 231603. <https://doi.org/https://doi.org/10.1016/j.jpowsour.2022.231603>.
- [14] Y. Cheng, Z. Wang, J. Chen, Y. Chen, X. Ke, D. Wu, Q. Zhang, Y. Zhu, X. Yan, M. Gu, Z. Guo, Z. Shi, *Angew. Chem. Int. Ed.* **2023**, *62*(30), e202305723. <https://doi.org/https://doi.org/10.1002/anie.202305723>.
- [15] X. Xie, J. Chen, X. Chen, Z. Shi, *J. Electroanal. Chem.* **2023**, *949*, 117862. <https://doi.org/https://doi.org/10.1016/j.jelechem.2023.117862>.
- [16] L. Pan, F. Liu, T. Xiang, C. Dong, T. You, Y. Zhang, C. Wang, L. Li, *Surfaces and Interfaces* **2024**, *54*, 105124. <https://doi.org/https://doi.org/10.1016/j.surfin.2024.105124>.
- [17] H. Song, J. Lee, M. Sagong, J. Jeon, Y. Han, J. Kim, H. G. Jung, J. S. Yu, J. Lee, I. D. Kim, *Adv. Mater.* **2024**, e2407381. <https://doi.org/https://doi.org/10.1002/adma.202407381>.
- [18] K. R. Adair, M. Iqbal, C. Wang, Y. Zhao, M. N. Banis, R. Li, L. Zhang, R. Yang, S. Lu, X. Sun, *Nano Energy* **2018**, *54*, 375–382. <https://doi.org/https://doi.org/10.1016/j.nanoen.2018.10.002>.
- [19] Y. Liang, Y. Chen, X. Ke, Z. Zhang, W. Wu, G. Lin, Z. Zhou, Z. Shi, *J. Mater. Chem. A* **2020**, *8*(35), 18094–18105. <https://doi.org/https://doi.org/10.1039/D0TA04768F>.
- [20] Y. Chen, X. Ke, Y. Cheng, M. Fan, W. Wu, X. Huang, Y. Liang, Y. Zhong, Z. Ao, Y. Lai, G. Wang, Z. Shi, *Energy Storage Mater.* **2020**, *26*, 56–64. <https://doi.org/https://doi.org/10.1016/j.ensm.2019.12.023>.
- [21] Y. Cheng, X. Ke, Y. Chen, X. Huang, Z. Shi, Z. Guo, *Nano Energy* **2019**, *63*, 103854. <https://doi.org/https://doi.org/10.1016/j.nanoen.2019.103854>.
- [22] C. Wei, Z. Yao, J. Ruan, Z. Song, A. Zhou, Y. Song, D. Wang, J. Jiang, W. Wang, J. Li, *Chin. Chem. Lett.* **2024**, *35*(3), 109330. <https://doi.org/https://doi.org/10.1016/j.ccl.2023.109330>.
- [23] Y. Deng, J. Gao, M. Wang, C. Luo, C. Zhou, M. Wu, *Energy Storage Mater.* **2022**, *48*, 114–122. <https://doi.org/https://doi.org/10.1016/j.ensm.2022.01.037>.
- [24] L. Gao, C. Sun, X. Li, Y. An, J. Li, Y. Bai, X. Bian, *Chem. Eng. J.* **2024**, *496*, 153444. <https://doi.org/https://doi.org/10.1016/j.cej.2024.153444>.
- [25] Q. Liu, R. Wang, Z. Liu, X. Wang, C. Han, H. Liu, B. Li, *J. Mater. Chem. A* **2023**, *11*(24), 12910–12917. <https://doi.org/https://doi.org/10.1039/D2TA09316B>.
- [26] P. Qing, Z. Wu, A. Wang, S. Huang, K. Long, T. Naren, D. Chen, P. He, H. Huang, Y. Chen, L. Mei, L. Chen, *Adv. Mater.* **2023**, *35*(15), 2211203. <https://doi.org/https://doi.org/10.1002/adma.202211203>.
- [27] G. Guo, K. Zhang, K. Zhu, P. Yang, Z. Shao, S. Liu, L. Lin, W. Zhuang, P. Xue, Q. Zhang, Y. Yao, *Adv. Funct. Mater.* **2024**, *34*(38), 2402490. <https://doi.org/https://doi.org/10.1002/adfm.202402490>.
- [28] T. Zhou, Y. Mu, J. Wu, B. Zhong, C. Yang, Q. Wang, W. Liu, H. Zhou, P. Jiang, *Chin. Chem. Lett.* **2022**, *33*(4), 2165–2170. <https://doi.org/https://doi.org/10.1016/j.ccl.2021.10.051>.

- [29] X. Liu, Q. Zhang, Y. Ma, Z. Chi, H. Yin, J. Liu, J. Huang, Z. Guo, L. Wang, *J. Energy Chem.* **2022**, *69*, 270–281. <https://doi.org/https://doi.org/10.1016/j.jechem.2021.12.046>.
- [30] Z. Luo, Y. Cao, G. Xu, W. Sun, X. Xiao, H. Liu, S. Wang, *Carbon Neutralization* **2024**, *3*(4), 647–672. <https://doi.org/https://doi.org/10.1002/cnl2.147>.
- [31] Y. Liu, C. Sun, Y. Lu, X. Lin, M. Chen, Y. Xie, C. Lai, W. Yan, *Chem. Eng. J.* **2023**, *451*, 138570. <https://doi.org/https://doi.org/10.1016/j.cej.2022.138570>.
- [32] C. Sun, L. Gao, W. Rong, R. Kang, Y. Yang, J. Li, Y. Bai, X. Tian, X. Bian, *Chem. Eng. J.* **2024**, *479*, 147821. <https://doi.org/https://doi.org/10.1016/j.cej.2023.147821>.
- [33] Z. Hou, Y. Yu, W. Wang, X. Zhao, Q. Di, Q. Chen, W. Chen, Y. Liu, Z. Quan, *ACS Appl. Mater. Interfaces* **2019**, *11*(8), 8148–8154. <https://doi.org/10.1021/acsmami.9b01521>.
- [34] X. Ke, Y. Liang, L. Ou, H. Liu, Y. Chen, W. Wu, Y. Cheng, Z. Guo, Y. Lai, P. Liu, Z. Shi, *Energy Storage Mater.* **2019**, *23*, 547–555. <https://doi.org/https://doi.org/10.1016/j.ensm.2019.04.003>.
- [35] A. Amardeep, D. J. Freschi, L. Sang, J. Liu, *Advanced Energy and Sustainability Research* **2024**, *5*(9), 2400035. <https://doi.org/https://doi.org/10.1002/aesr.202400035>.
- [36] S. Xia, X. Zhang, H. Zhao, J. Xie, L.-Y. Chou, Y. Yu, W. Liu, *Small* **2020**, *16*(20), 2001257. <https://doi.org/https://doi.org/10.1002/smll.202001257>.
- [37] C. Guo, Y. Guo, R. Tao, X. Liao, K. Du, H. Zou, W. Zhang, J. Liang, D. Wang, X.-G. Sun, S.-Y. Lu, *Nano Energy* **2022**, *96*, 107121. <https://doi.org/https://doi.org/10.1016/j.nanoen.2022.107121>.
- [38] T. Liu, J. Hu, C. Li, Y. Wang, *ACS Appl. Energ. Mater.* **2019**, *2*(6), 4379–4388. <https://doi.org/10.1021/acsamem.9b00573>.
- [39] S. Park, H.-J. Jin, Y. S. Yun, *Adv. Mater.* **2020**, *32*(51), 2002193. <https://doi.org/https://doi.org/10.1002/adma.202002193>.
- [40] S. Li, X.-S. Wang, Q.-D. Li, Q. Liu, P.-R. Shi, J. Yu, W. Lv, F. Kang, Y.-B. He, Q.-H. Yang, *J. Mater. Chem. A* **2021**, *9*(12), 7667–7674. <https://doi.org/10.1039/DITA00408E>.
- [41] G. Liu, Y. Li, L. Zhang, H. Tao, X. Yang, *Appl. Surf. Sci.* **2023**, *620*, 156809. <https://doi.org/https://doi.org/10.1016/j.apsusc.2023.156809>.
- [42] Q. Ran, H. Zhao, J. Liu, L. Li, Q. Hu, J. Song, X. Liu, S. Kormarneni, *J. Energy Chem.* **2023**, *83*, 612–621. <https://doi.org/https://doi.org/10.1016/j.jechem.2023.04.047>.
- [43] K. Yu, J. Chen, X. Xie, K. Lin, J. Li, Z. Shi, *Surfaces and Interfaces* **2022**, *34*, 102326. <https://doi.org/https://doi.org/10.1016/j.surfin.2022.102326>.
- [44] Y. Yu, K. Long, S. Huang, S. Yu, J. Yang, T. Naren, Y. Chen, W. Wei, X. Ji, B. Ju, G.-C. Kuang, L. Chen, *Adv. Funct. Mater.* *n/a(n/a* 2424386. <https://doi.org/https://doi.org/10.1002/adfm.202424386>.
- [45] H. Wang, D. Lin, Y. Liu, Y. Li, Y. Cui, *Sci. Adv.* **2017**, *3*(9), e1701301. <https://doi.org/doi:10.1126/sciadv.1701301>.
- [46] Z. Wang, T. Chen, Y. Liu, J. Xing, A. Zhou, J. Li, W. Zou, F. Zhou, *Chem. Eng. J.* **2022**, *430*, 132970. <https://doi.org/https://doi.org/10.1016/j.cej.2021.132970>.
- [47] Y. Chen, Q. Zhang, K. Wang, M. Shen, L. Zhang, Y. Li, J. Yuan, A. Wang, F. Shen, X. Han, *ACS Appl. Mater. Interfaces* **2024**, *16*(22), 28570–28577. <https://doi.org/10.1021/acsmami.4c04070>.
- [48] S. Ye, X. Chen, R. Zhang, Y. Jiang, F. Huang, H. Huang, Y. Yao, S. Jiao, X. Chen, Q. Zhang, Y. Yu, *Nano-Micro Lett.* **2022**, *14*(1), 187. <https://doi.org/10.1007/s40820-022-00932-3>.
- [49] L. Tan, P. Chen, Q.-Y. Chen, X. Huang, K.-Y. Zou, Y.-M. Nie, L.-J. Li, *Rare Met.* **2023**, *42*(12), 4081–4090. <https://doi.org/10.1007/s12598-023-02416-8>.
- [50] C. Ma, F. Xu, T. Song, *ACS Appl. Mater. Interfaces* **2022**, *14*(17), 20197–20207. <https://doi.org/10.1021/acsmami.2c00842>.
- [51] X. Chu, F. Dong, X. Zhang, Y. Liu, Y. Jiang, H. Xie, *J. Energy Storage* **2024**, *94*, 112447. <https://doi.org/https://doi.org/10.1016/j.est.2024.112447>.
- [52] S. Guo, L. Wang, Y. Jin, N. Xiao, Z. Chen, G. Tian, J. Li, C. Zhao, X. He, *Nano Convergence* **2020**, *7*(1), 21. <https://doi.org/10.1186/s40580-020-00231-w>.

Manuscript received: January 15, 2025

Revised manuscript received: February 18, 2025

Accepted manuscript online: March 4, 2025

Version of record online: March 25, 2025